A Discovery of Strong Metal-Support Bonding in Nano-engineered Au-Fe_3O_4 Dumbbell-like Nanoparticles by *In-situ* Transmission Electron Microscopy

Chang Wan Han[1,2], Tej Choksi[3], Cory Milligan[2,3], Paulami Majumdar[3], Michael Manto[4], Yanran Cui[3], Xiahan Sang[5], Raymond R Unocic[5], Dmitry Zemlyanov[2], Chao Wang[4], Fabio H Ribeiro[3], Jefferey Greeley[3] and Volkan Ortalan[1,2]*

1. School of Materials Engineering and Birck Nanotechnology Center, Purdue University, West Lafayette, IN, USA
2. Birck Nanotechnology Center, Purdue University, West Lafayette, IN, USA
3. School of Chemical Engineering, Purdue University, West Lafayette, IN, USA
4. Department of Chemical and Biomolecular Engineering, Johns Hopkins University, Baltimore, MD, USA
5. Center for Nanophase Materials Science, Oak Ridge National Laboratory, Oak Ridge, TN, USA

KEYWORDS Heterogeneous catalysis, Gold catalyst, Metal-Support Interaction, Electron microscopy, Density Functional Theory

ABSTRACT

The strength of metal-support bonding in heterogeneous catalysts determines their thermal stability, therefore, a tremendous amount of effort has been expended to understand metal-support interactions. Herein, we report the discovery of an anomalous “strong metal-support bonding”

between gold nanoparticles and "nano-engineered" Fe_3O_4 substrates by *in-situ* microscopy. During *in-situ* vacuum annealing of Au-Fe_3O_4 dumbbell-like nanoparticles, synthesized by the epitaxial growth of nano-Fe_3O_4 on Au nanoparticles, the gold nanoparticles transform into the gold thinfilms and wet the surface of nano-Fe_3O_4, as the surface reduction of nano-Fe_3O_4 proceeds. This phenomenon results from a unique coupling of the size-and shape-dependent high surface reducibility of nano-Fe_3O_4 and the extremely strong adhesion between Au and the reduced Fe_3O_4. This strong-metal support bonding reveals the significance of controlling the metal oxide support size and morphology for optimizing metal-support bonding and, ultimately, for the development of improved catalysts and functional nanostructures.

TOC Graphic

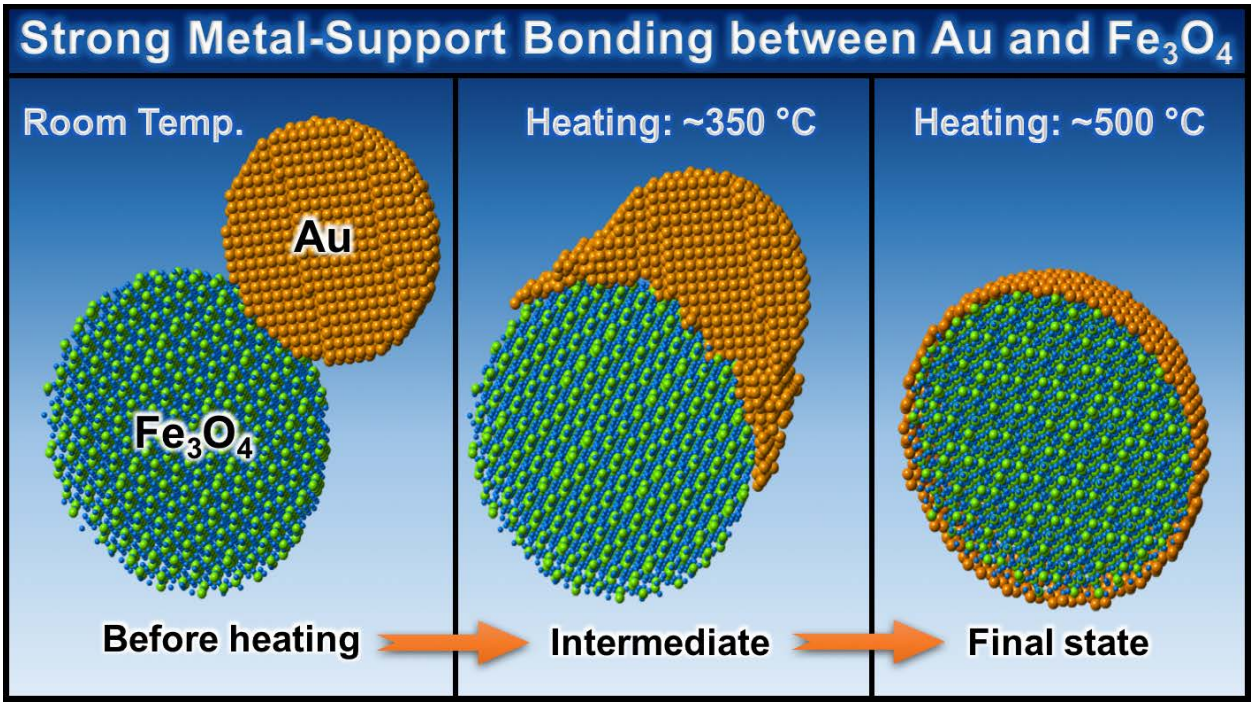

Metal nanoparticles (NPs) supported on an oxide substrate are among the most important types of heterogeneous catalysts for producing chemical products and for exhaust gas clean-up. It has long been known that, in many cases, the catalytic performances, including the activity, selectivity, and stability, is strongly dependent both on the supported metal NPs themselves and on the metal support interactions. Since the metal support interaction can dramatically change the catalytic properties, many efforts have been made to understand and utilize the interaction for the real catalytic applications.

Among the parameters determining the catalytic properties, the strength of the metal-support bonding (MSB) is of the utmost importance for the industrial heterogeneous catalysts because the MSB directly determines the stability (lifetime) of the supported catalytic metal NPs.[1] This is especially critical for the supported gold catalysts owing to their low sintering resistance. Since the discovery of the high catalytic activity of gold NP catalysts for low temperature CO oxidation,[2,3] gold catalysts have been extensively studied for various chemical processes for which they showed excellent catalytic activities.[4] Despite the high potential of the gold catalysts for greener chemical processes, however, rapid deactivation of them by sintering of the gold NPs limits the realization of a wide range of industrial applications of the supported gold catalysts.[5,6]

Over the past two decades, although, there have been various studies on the MSB between gold and metal oxide supports showing not only high catalytic activities[7–9] but also high stability[10] against sintering, no attempts to understand the observed catalytic improvements[11,12]—whether activity or selectivity—at the molecular level, to elucidate the fundamental physicochemical factors that govern the metal/oxide interaction, or to generalize the fundamental understanding to various metal/oxide systems, have been reported, and such information is required to ultimately design the next generation of functional nanocatalysts.

Here, we report *in-situ* transmission electron microscopy (TEM), electron and X-ray spectroscopies, and density functional theory (DFT) results showing a direct experimental evidence of the strong metal-support bonding (SMSB) between gold and iron oxide in the Au-Fe_3O_4 dumbbell nanoparticles (DNPs), where the average diameters of the Au NPs and the Fe_3O_4 NPs are 5.0 nm and 10.4 nm, respectively. Drastic morphological changes of Au NP from a spherical NP to Au thinfilm (i.e., complete wetting) on Fe_3O_4 during the vacuum annealing directly indicates the presence of SMSB between Au and Fe_3O_4 during the *in-situ* annealing experiment. This result also emphasizes the importance of the precise control of the metal oxide supports in rational design of a stable gold catalyst. To the best of our knowledge, this is the first discovery of the SMSB in gold-iron oxide system and it generalizes the results and provides molecular-level explanations that could be applicable to many different systems.

Au-Fe_3O_4 DNPs were prepared by initiating the epitaxial growth of Fe on Au NP seeds followed by Fe oxidation in an organometallic solution synthesis[13–15]. Organic methods of synthesis were employed to tightly regulate the size distribution of the nanoparticles and to direct the controlled growth of Fe_3O_4 on the exposed (111) facets of the Au seeds.

In-situ TEM and STEM videos and images were collected both at 300 kV and 60 kV using a probe aberration-corrected FEI Titan-S 80-300 equipped with a Gatan OneView CMOS camera and a Protochips Aduro heating stage at Oak Ridge National Laboratory. *In-situ* STEM-EELS were performed at 300 kV on an FEI Titan ETEM 80-300 equipped with a Gatan Tridiem GIF and Gatan single tilt 752 heating stage. XPS spectra were obtained by a Kratos Axis Ultra DLD spectrometer with monochromatic Al Kα radiation (1486.6 eV) at pass energy of 20 and 160 eV for high-resolution and survey spectra, respectively.

Periodic DFT calculations were performed with VASP[16–18] using the projector augmented wave method (PAW)[19–21] for Fe_2O_3 (0001), Fe_3O_4 (111), FeO (111) and Fe (110) surfaces. Au nanoparticles are modeled as Au (111) films with pseudomorphic registry on the iron oxides and a moiré pattern on Fe (110). Geometries of the models are shown in Figure 4 (b) (see SI for more details). Self-consistent electronic energies are calculated using the PBE functional[22,23] within the generalized gradient approximation (GGA). The GGA+U[24,25] approach is employed to partially correct the self-interaction error prevalent in standard GGA functionals like PBE. The specific implementation of DFT+U used in this work follows Dudarev *et al*.[26,27] Electronic cores of Fe, O and Au are represented by PAW PBE pseudopotentials. Further details, including kinetic energy cutoffs, k-points based on the Monkhorst Pack scheme,[28] magnetization and the numerical tolerances employed for iterative solutions of the Kohn Sham equations, are provided in the SI. An *ab initio* phase diagram analysis indicating the thermodynamic stability of iron oxide surfaces with and without Au films, based on the method proposed by Reuter and Scheffler,[29] is also reported in the Supplementary Information.

Figure 1 shows snapshots of the *in-situ* TEM movie (Movie S1) summarizing the thermal behaviors and morphological changes (i.e., wetting) of the Au-Fe_3O_4 DNPs and Au NPs with increasing temperature. Au NPs were intentionally mixed with the DNPs with the aim of comparing the thermal behaviors of the DNPs and Au NPs (marked with dotted line in Figure 1a). The Au-Fe_3O_4 DNPs were gradually heated up from room temperature up to 550 °C under high vacuum (1.88×10^{-7} Torr) with the heating profile (time vs. temperature) of the *in-situ* TEM experiment presented in Figure 1g.

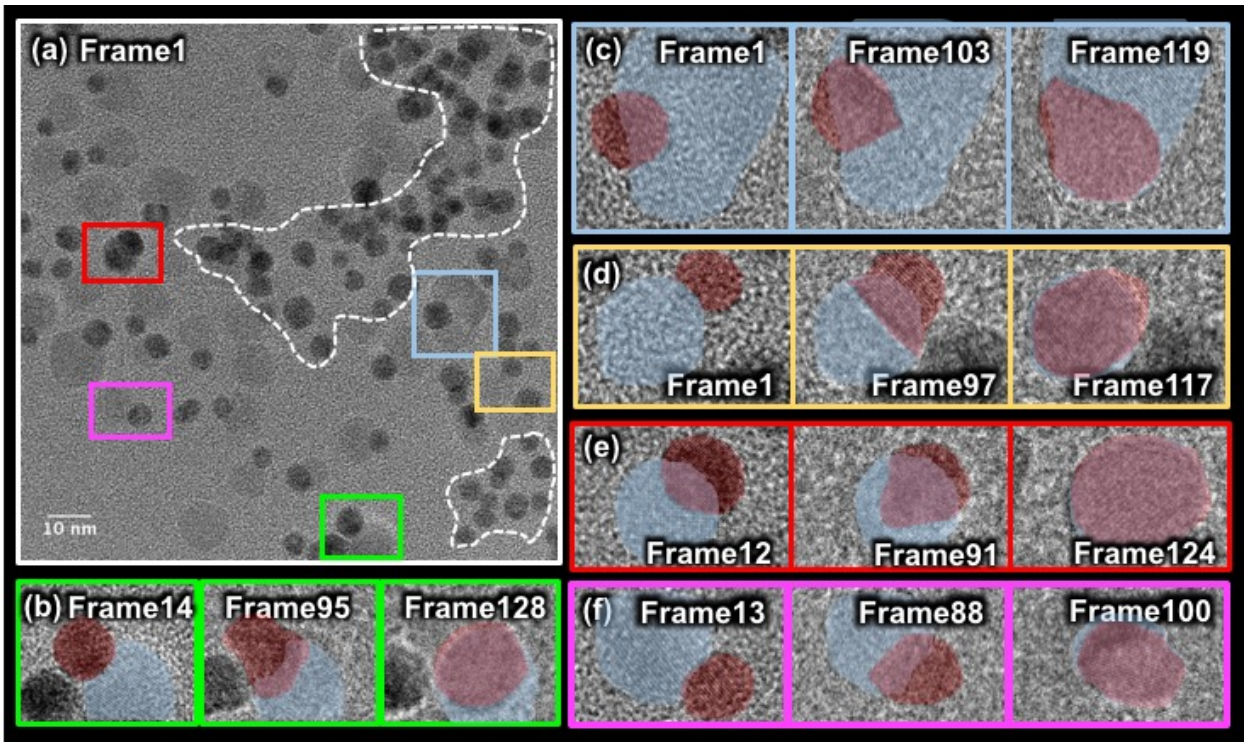

Figure 1. Snapshots of an *in-situ* heating TEM movie summarizing the thermal behavior of Au-Fe_3O_4 DNPs. (a**)** The initial frame taken at ~ 100 degree °C (b)-(f) Sequential snapshots showing the wetting behaviors of Au NPs on iron oxide domains. For better visibility, Au and Fe_3O_4 are false colored as transparent red and blue, respectively. (g) Temperature vs. time profile of the annealing experiment.

With increasing annealing temperature from room temperature to ~ 350 °C, a neck formation between regular Au NPs (without Fe_3O_4), which is the first step of sintering process, was observed. As the temperature was further increased, the regular Au NPs coalesced and formed several bigger Au particles. However, the gold domain of the DNPs started to flatten and partially covered the surface of the iron oxide domains at ~ 350 °C (Figure 1b-f). As the wetting process proceeded, the iron oxide domain was totally covered by the gold thin-film at ~ 500 °C. The thickness of the flattened Au on iron oxide was calculated as 1.9 Å, which corresponds to one monolayer of Au film on an iron oxide NP, assuming the shape of Au and Fe_3O_4 are spherical and their volumes are conserved during the entire heating experiment (Figure S1).

The observed structures of gold thinfilm on a Fe_3O_4 domain indicate that SMSB were formed at the interface between Au and Fe_3O_4 during the *in-situ* annealing. This result implies that the metal-substrate (Au-Fe_3O_4) interfacial adhesion is stronger than the metal-metal (Au-Au) bonds, which is related to the surface tension of the Au NP. This is surprising, because it is contradictory to the well-known fact that a gold film grown on an extended surface of a single-crystalline Fe_3O_4 substrate at high temperatures (400°C and 750°C) has a 3D island shape rather than a 2D film structure,[30,31] which corresponds to a Volmer-Weber growth mode, wherein the strength of the interfacial adhesion is weaker than gold-gold bonds. The change in strength of the MSB between the Au-Fe_3O_4 DNPs during annealing can be estimated by calculating the adhesion energy using Young-Dupré equation (Eq. 1).

$$E_{adh} = \gamma_{np}(1-\cos\theta) \quad \ldots \text{Equation 1.}$$

where γ_{np} and θ are the surface tension of the supported nanoparticle and the contact angle, respectively.

In our case of a gold thin film on an iron oxide nanoparticle where theta equals 180°, the surface tension is estimated as 2.56 J/m^2 ($2\times\gamma_{Au(111)}$) and this value is 0.26 J/m^2 higher than the previously reported value of Au(111)/Fe_3O_4(111) (2.3 J/m^2) reported elsewhere.[32]

The major structural difference between the Au-Fe_3O_4 DNPs and Au/single-crystalline Fe_3O_4 with an extended surface, which might be the reason for the directly-opposed wetting behavior, is the size and morphology of the nano-Fe_3O_4. In the case of the DNPs, the nano-Fe_3O_4 domain has an average diameter of only ~10 nm. Moreover, due to the large curvature of the nano-Fe_3O_4 domain, the chemical potential of the surface atoms on the spherical Fe_3O_4 with ~ 5 nm radius is much

higher compared to the extended flat Fe_3O_4, as predicted from the Gibbs-Thomson equation. This higher surface chemical potential possibly causes the surface to be more reactive and form a stronger adhesion with gold than the flat Fe_3O_4 surfaces.

Another remarkable difference between the nano-Fe_3O_4 of the DNPs and regular Fe_3O_4 is the facets enclosing the Fe_3O_4 crystal. In contrast to the regular Fe_3O_4, the nano-Fe_3O_4 domain in the DNPs are epitaxially grown on the Au NP seeds during the synthesis of the DNPs (see SI for the details of the sample preparation). Therefore, thermodynamically less favorable Fe_3O_4 (011) and (131) facets[33,34] can be formed along with Fe_3O_4 (111) due to the epitaxial relationship of Au and Fe_3O_4 (Au(220)[112]//Fe_3O_4(440)[112] and Au(111)[112]//Fe_3O_4(222)[112] with a ~2.7 % and ~3 % lattice mismatch, respectively) (Figure S2 a, b). The epitaxial facet development of Fe_3O_4 in the DNPs were also observed from the annular-dark field (ADF) electron tomography investigation (Figure S2, c. d). In this regard, we believe the energetically reactive facets of the DNPs might also contribute to the SMSB.

To investigate the changes in the local chemical nature of the DNPs during the vacuum annealing, we performed *in-situ* scanning TEM (STEM) electron energy loss spectroscopy (EELS) during annealing of the Au-Fe_3O_4 DNPs at 500 °C. Several different DNPs, which correspond to the "*initial*", "*intermediate*", and "*final*" state of the gold wetting/flattening process, were characterized. Figure 3 shows annular dark-field (ADF) STEM images of the DNP representing one of the aforementioned states along with the locally collected EEL spectra from the DNPs shown in the STEM images. The locations where EEL spectrum collections were performed, and the corresponding spectra, are color-coded accordingly.

The DNP before the flattening maintained its dumbbell shape and a noticeable phase

transformation, such as an intermixing between gold and iron oxide, was not observed (Figure 2a). However, as can be seen in Figure 2b where the hemisphere of iron oxide domain was partially covered by flattened gold, we found that the surface of the "gold covered" iron oxide hemisphere was heavily reduced. Consequently, the O K edge intensity was negligible. On the contrary, as it is evident from the EEL spectrum collected from DNPs, representative of the "intermediate" stage of the wetting process (green spectra in Fig. 2b), the portion of the iron oxide with no Au coverage (darker region of the DNP in Fig. 2b) remained as an oxide. The "final" state shown in Fig. 2c illustrates that the iron oxide is fully covered by the Au film while the core remained an oxide and the iron oxide surface was highly reduced. By considering these *in-situ* STEM-EELS results as well as *in-situ* electron diffraction results (Figure S3), it can be concluded that the core part of the final state still has a form of unreduced Fe_3O_4 and this suggests that the drastic morphology change of the DNPs is not due to the Au-Fe binary alloy particle formation but is due to the interaction between the Au thinfilm and the iron oxides.

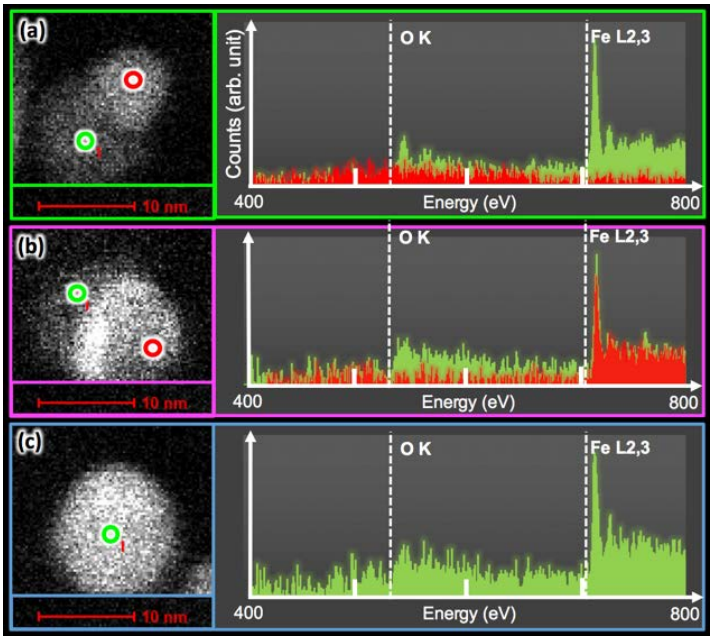

Figure 2. Results of *in-situ* STEM-EELS showing ADF-STEM images and EEL spectrum

collected from the DNPs at (a) "*initial*", (b) "*intermediate*", and (c) "*final*" state of the wetting/flattening process.

Furthermore, these results suggest that the SMSB in the Au-Fe_3O_4 DNPs is correlated with the surface reduction of the iron oxide domain. The role of surface oxygen vacancies of the metal oxides on MSB has been investigated by several researchers and it has been reported that the surface oxygen vacancies of CeO_2 and TiO_2 strongly stabilize metal NPs.[35,36] Moreover, it has also been pointed out that the amount of surface oxygen vacancies contributing to the strength of the MSB for oxide-enclosed metal nanoparticles is strongly dependent on the facets enclosing the support particles because the redox capability of a metal oxide is dependent upon the type of facets.[10,11,37] Therefore, we may conclude that the unique SMSB of the DNPs is due to the higher reducibility (or higher surface oxygen vacancy concentration) of nano-Fe_3O_4, having high surface chemical potentials and reactive facets, as discussed above. The SMSB with reduction of Fe_3O_4 is further investigated below through XPS and DFT based atomistic simulations.

In order to determine the oxidation states during the iron oxide reduction process, we performed X-ray photoelectron spectroscopy (XPS) analysis of the DNPs before and during vacuum annealing at 500 °C. The heating was performed *in-situ* in UHV allowing spectra to be obtained while the sample was held at 500 °C and one hour was given to equilibrate the system before beginning the acquisition. Before heating the sample, the Fe $2p_{3/2}$ main peak is located at 710.5 eV with no distinct shake up feature, which is characteristic of the convolution of the Fe^{3+} and Fe^{2+} features present in Fe_3O_4.[38] During the vacuum annealing, the centroid of the Fe $2p_{3/2}$ peak shifts to 709.3 eV and a distinct shake-up feature appears at 715.6 eV, as shown in Figure 3a. Both the peak position and the distance between the main peak and the shake-up indicate Fe^{2+} formation.[39]

Along with the reduction of Fe^{3+} to Fe^{2+}, a prominent feature representing approximately 30% of the total Fe 2p area appears at 706.8 eV, indicating the reduction to metallic iron. Accompanying the reduction of Fe, a shift in the Au $4f_{7/2}$ peak from 83.8 eV to 84.2 eV is seen, as shown in Figure 3b. This +0.4 eV chemical shift can be explained either by a size effect [40] (in our case, morphological changes observed in TEM) or by gold coordinating with iron forming an intermetallic phase, a similar shift as observed in the Au_xIn_y alloy system.[41]

This XPS result indicating the surface reduction of the nano-Fe_3O_4 hints at a fundamentally new phenomenon in metal/oxide nanoscience, involving a cooperative size- and metal-induced reduction of oxide nanoparticle surfaces. According to Syed *et al*.,[40] a100 nm thick Fe_3O_4 thin film deposited on Si substrate was completely stable against the reduction in the vacuum annealing (from 573 K to 973 K at 9.75×10^{-7} Torr) and therefore, the Fe 2p3/2 peak in the XPS spectra remained on the same binding energy. Also, a characteristic peak indicating a metallic Fe has never appeared.[40] This suggests that the spherical nano-Fe_3O_4 has a higher reducibility and a higher capability of containing oxygen vacancies on its surface compared to flat extended Fe_3O_4. As already observed from *in-situ* STEM-EELS, the SMSB and the gold wetting behavior are closely related to the surface reduction of Fe_3O_4. In order to further verify that this reduction is likely due to nanosize effect, we also conducted XPS on 5 µm Fe_3O_4 (bulk) treated using the same conditions as the DNPs. As shown in Figure 3a, the XPS spectra collected after vacuum annealing were consistent with bulk Fe_3O_4, containing both Fe^{3+} and Fe^{2+} peaks of appropriate intensity with no distinct shake-up or metallic iron features. This compelling result strongly suggests that nanosize effects contribute to the reducibility of the iron oxide particles.

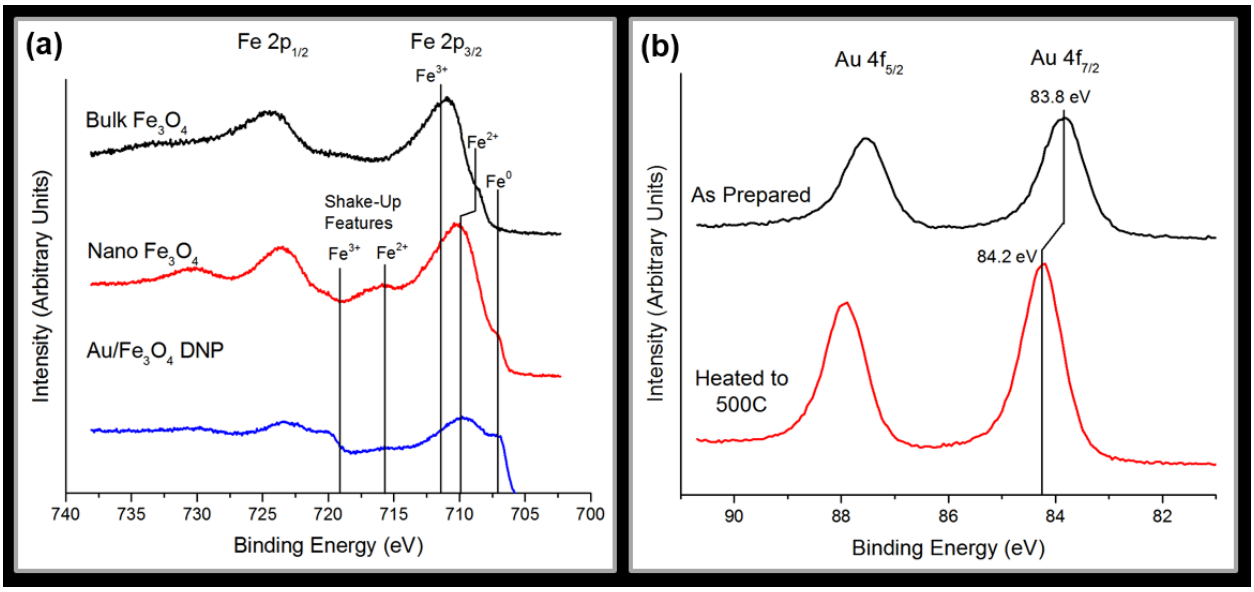

Figure 3. XPS measurement. (a) Fe 2p spectra collected at 500 °C for bulk Fe_3O_4, nano-Fe_3O_4, and Au/Fe_3O_4 DNPs. Reference lines for the features are shown to help guide the eyes and are taken from Ref. [39]. (b) Au 4f spectra from the Au/Fe_3O_4 DNPs taken as prepared and after annealing to 500 °C.

A similar XPS experiment was performed on the nano-Fe_3O_4 NPs synthesized without gold to determine if the reduction behavior is exclusively due to the size effect of the nano-Fe_3O_4 or if gold plays an important role in the observed reduction phenomena. The spectra of the nano-Fe_3O_4, shown in Figure 3a, obtained from before heating and *in situ* are qualitatively similar to the Au-Fe_3O_4 DNPs, in terms of the peak positions and the shake-up features. Both show a reduction of Fe_3O_4 to FeO and Fe, but the difference arises in the relative concentration of the metallic iron formed. As shown in Figure 3a (red line), without the presence of gold, only 7.5% of the total iron signal appears as metallic iron compared to the 30% when gold is present (Figure 3a blue line). These results prove that the nano-Fe_3O_4 is reducible even without gold, however, gold substantially

accelerates the reduction phenomena. This effect is further analyzed below with DFT calculations on FeO, which represents a partially reduced iron oxide support. These results strongly imply that a novel, concerted nanosize- and metal-dependent reduction phenomena must exist to produce the observed difference in the reducibility between the nano-Fe_3O_4 and the extended Fe_3O_4.

TEM and XPS studies highlight the SMSB between Au and Fe_3O_4 in DNPs, as evidenced by wetting of Au nanoparticles during in situ annealing experiments. Furthermore, experimental results demonstrate that the SMSB is observed with a concomitant reduction of the iron oxide surface. To provide an atomic-level description and interpretation of this phenomenon, we performed first principles Density Functional Theory (DFT) calculations of the gold/iron oxide interface. The interaction between progressively reduced iron oxide supports and Au nanoparticles was studied through a trend based analysis of the stability of Au (111) films on a range of extended iron oxide surfaces, with a variety of oxidation states, including Fe_2O_3 (0001), Fe_3O_4 (111), FeO (111), and Fe (110) surfaces, in order of decreasing iron oxidation state. The Au (111) films possess a pseudomorphic registry on Fe_2O_3 (0001), Fe_3O_4 (111) and FeO (111), while the film is modeled as a moiré pattern on Fe (110) to minimize strain effects (further details regarding lattice registries between films and substrates are presented in the SI). As DFT calculations of Au/Fe_3O_4 nanoparticles are computationally intractable, extended surface models are employed to provide approximate treatments of the gold/iron oxide interface, and thereby describe trends in how gold facilitates the reduction of the DNPs as nanoparticle.

Binding energies ($E^{binding}$) of Au films on the oxygen- and iron-terminated surfaces of iron oxide models (Equation 2), reflecting heats of adsorption of Au films on iron oxide substrates, are shown in Figure 4(a). The binding energies are referenced to bulk FCC Au.

$$E^{binding} = \frac{E_{Au\ on\ FexOy} - E_{FexOy} - N_{Au}E_{Au\ atom\ in\ bulk}}{N_{Au\ on\ surface}} \ldots \text{Equation 2.}$$

where E_i is the DFT calculated ground state energy of system *i*, and N_{Au} is number of Au atoms. A more negative value of the binding energy indicates stronger binding.

The total energy of bulk Au is corrected for nanoparticle size effects using the Gibbs–Thompson relation (see Supporting Information). The binding energy of Au (111) on the iron terminated (oxygen terminated) surfaces is represented on the right (left) for each iron oxide substrate in Figure (4a). Adsorption energies of surfaces terminated by mixtures of iron and oxygen atoms, which are between the two limiting cases discussed in Fig. 4 (a), are reported in SI. Au (111) interacts very weakly with the O terminated surface, as evidenced by the positive binding energies. In contrast, the adsorption energy of Au (111) on iron-terminated surfaces is quite exothermic, being -0.37 eV for Fe_2O_3 (0001), -0.20 eV for Fe_3O_4 (111), -0.80 eV for FeO (111) and -0.64 eV for Fe (110), where the energies have been normalized per gold atom at the interface. Moreover, the monotonic decrease in the binding energy of Au (111) with supports containing progressively lower iron oxidation states shows increased interaction between Au and the iron oxide surface upon reduction. Such a trend is fully consistent with the electron microscopy and XPS observations which report a flattening of Au nanoparticles and concomitant reduction of the Au/iron oxide interface with increasing temperature.

DFT calculations were further combined with thermodynamic relations to construct *ab initio* phase diagrams of Au films supported on Fe_2O_3 (0001), Fe_3O_4 (111), and FeO (111) (see Supporting Information). The phase diagrams show that, at low oxygen chemical potentials (representing high temperatures and low oxygen partial pressures), Au (111) films on reduced iron oxide are the thermodynamically most stable phase, while at higher oxygen chemical potentials, the bare iron

oxide supports show the highest stability. This result is also in line with the experimental observations that flattening of Au nanoparticles occurs at higher temperatures. Finally, the calculations show that the oxygen vacancy formation energy for FeO (111), which is the phase present immediately prior to metallic iron formation and full gold wetting, is lowered by 0.74 eV in the presence of an Au film, indicating that the formation of oxygen vacancy in FeO (111) becomes significantly more favorable in presence of Au. This evidence, concurrent with XPS results, demonstrate that Au NPs accelerate the latter stages of the reduction of iron oxide.

Overall, DFT calculations show progressively stronger binding of Au films with the reduction of the iron oxide support. The phase diagrams further confirm stability of Au films under a reducing environment with increasing temperature. Thus, stronger adhesion of thin films on reduced iron oxide and more favorable oxygen vacancy formation in the presence of Au lead to the increased stability of Au thin films on reduced iron oxide surfaces at high temperatures. DFT-based atomistic calculations therefore strongly support the SMSB between Au and Fe_3O_4 DNPs, as evidenced by the flattening of Au NPs through the *in-situ* TEM experiment.

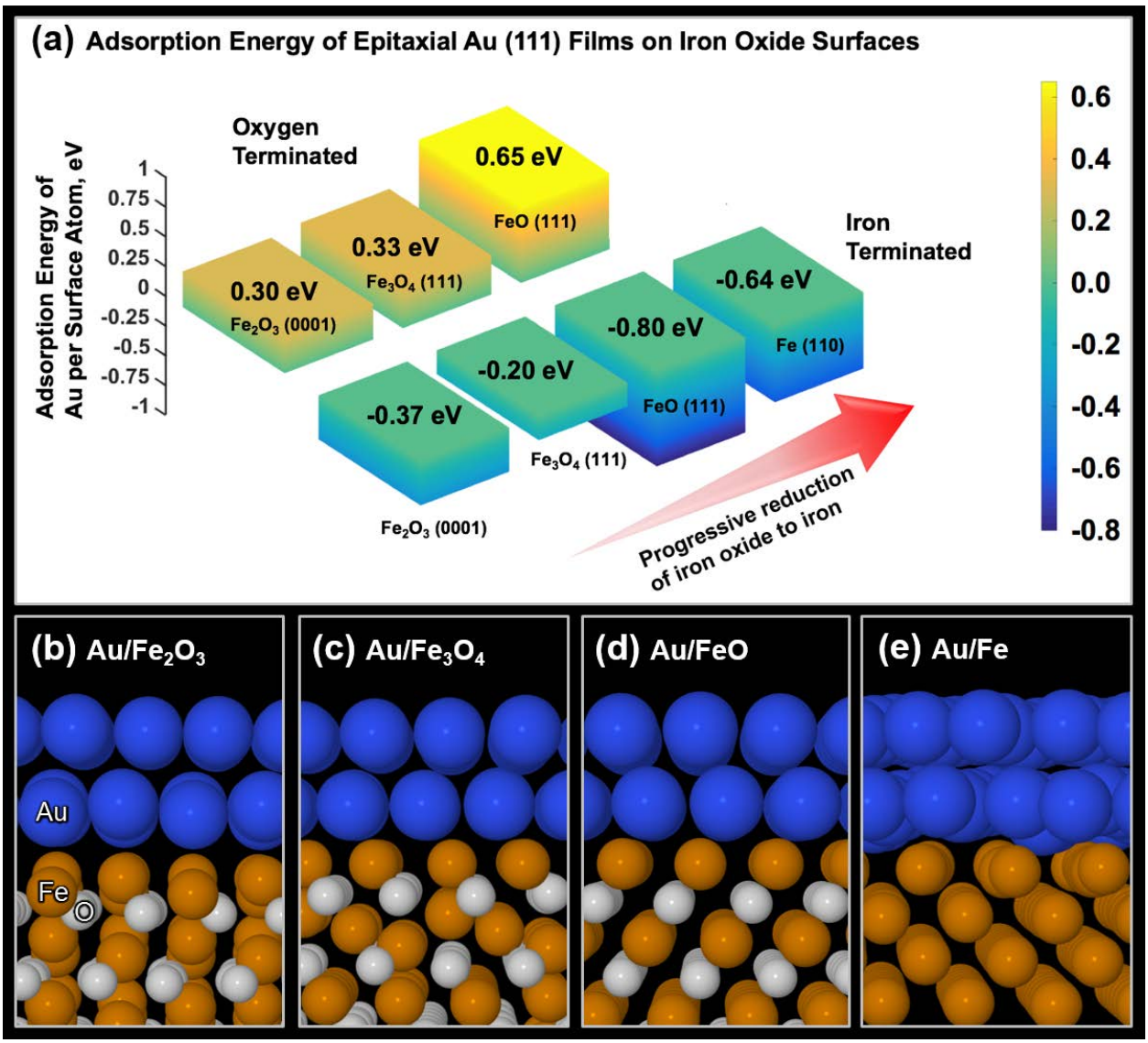

Figure 4. DFT calculation results. (a) Trends in adsorption energies of epitaxial Au (111) films as iron oxide is progressively reduced from Fe_2O_3 to Fe. Binding on the iron terminated surfaces (bars in the right) is significantly more favorable in comparison with oxygen terminated surfaces (bars in the left). The monotonic reduction in binding energy with reduction of iron oxide confirms experimental observations regarding an increase in wetting/SMSB between Au and iron oxide during in situ annealing. Binding energies are normalized by the number of gold atoms present at the interface. (b) 2 monolayered (ML) Au film supported on the 2-Fe termination of Fe_2O_3 (0001).

(c) 2 ML Au film supported on the oct-1 Fe_3O_4 (111) termination. (d) 2 ML Au film adsorbed on Fe-terminated FeO (111) surface. (e) 2 ML Au (111) film adsorbed on the metallic Fe (110) surface (see SI for more information about adsorption configurations). Au, Fe, and O atoms are depicted in yellow, brown, and red, respectively.

In summary, we have employed a combination of *in-situ* TEM, XPS, and DFT calculations to obtain a mechanistic understanding of the wetting behavior of the gold nanoparticles in dumbbell-like nanoparticle (DNP) assemblies with completely gold covered iron oxide domains during high temperature annealing. This drastic morphological change of Au is a direct evidence of SMSB between gold and iron oxide, which occurred during the vacuum annealing. The origin of the SMSB is attributed to a combination of the higher reducibility and higher concentration of the surface oxygen vacancies of the spherical nano-Fe_3O_4 (i.e., iron oxide domains of the DNPs) and to the direct interaction of the Au NP's with the iron oxide surface. *In-situ* STEM-EELS showed that the Au covered part of the nano-Fe_3O_4 was highly reduced. XPS experiments showed that the nano-Fe_3O_4 NPs were readily reduced during the vacuum annealing, while extended Fe_3O_4 thin films were highly stable against surface reduction. A series of our experimental results suggests a strong correlation between the wetting/SMSB and the surface reduction. DFT calculations further revealed that (1) thin Au films possess a stronger bonding to the iron oxide support with increasing reduction and (2) Au accelerates the vacancy formation in DNPs, thereby strongly supporting the experimentally observed wetting of Au nanoparticles on reduced iron oxide supports.

The SMSB observed in the Au-Fe_3O_4 DNPs is not only physically interesting but also practically

important because it emphasizes the significance of the size and morphology control of a metal oxide support for tuning the metal-support bonding. Moreover, it opens up a novel way for preparing highly stable Au catalysts by optimizing the support size. In this regard, we believe that it is imperative to revisit the commonly utilized metal oxide supports and carefully investigate their size dependent properties owing to the fact that the metal-support interaction can potentially be very different with respect to the morphology and the size of materials, as we here observed. More importantly, this work demonstrates the prominence of nano-engineering to develop novel material systems ultimately for the development of improved catalysts and tunable and highly stable functional nanostructures for other applications, such as energy storage and conversion devices.

Supporting Information. Supporting Information containing the detailed experimental methods, computational details and gold/iron oxide adsorption configurations and *ab initio* phase diagrams is available online. Supporting information also contains *in-situ* TEM movie summarizing the thermal behaviors of Au-Fe_3O_4 dumbbell-like nanoparticles (Movie S1).

AUTHOR INFORMATION

Corresponding Author

*E-mail: vortalan@purdue.edu

ACKNOWLEDGEMENT

This work was supported by the Designing Materials to Revolutionize and Engineer our Future (DMREF) program of the National Science Foundation (CBET-1437219). *In-situ* TEM data were

collected using the FEI Titan S 80-300 TEM/STEM at the Center for Nanophase Materials Sciences, which is a DOE Office of Science User Facility. We also thank Prof. E. P. Kvam for critically reading the manuscript.

References

(1) Farmer, J. A.; Campbell, C. T. *Science (80-.).* **2010**, *329* (August), 933–936.

(2) Hutchings, G. J. *J. Catal.* **1985**, *96* (1), 292–295.

(3) Haruta, M.; Kobayashi, T.; Sano, H.; Yamada, N. *Chem. Lett.* **1987**, No. 2, 405–408.

(4) Hashmi, A. S. K.; Hutchings, G. J. *Angew. Chemie - Int. Ed.* **2006**, *45* (47), 7896–7936.

(5) Choudhary, T. V.; Goodman, D. W. *Top. Catal.* **2002**, *21* (1–3), 25–34.

(6) Bokhimi, X.; Zanella, R.; Angeles-Chavez, C. *J. Phys. Chem. C* **2010**, *114*, 14101–14109.

(7) Fu, Q.; Weber, A.; Flytzani-Stephanopoulos, M. *Catal. Letters* **2001**, *77* (1–3), 87–95.

(8) Fu, Q.; Saltsburg, H.; Flytzani-stephanopoulos, M. *Science (80-.).* **2003**, *301* (August), 935–938.

(9) Rodriguez, J. A.; Ma, S.; Liu, P.; Hrbek, J.; Evans, J.; Pérez, M. *Science (80-.).* **2007**, *318* (December), 1757–1760.

(10) Ta, N.; Liu, J.; Chenna, S.; Crozier, P. A.; Li, Y.; Chen, A.; Shen, W. *J. Am. Chem. Soc.* **2012**, *134*, 20585–20588.

(11) Boucher, M. B.; Goergen, S.; Yi, N.; Flytzani-Stephanopoulos, M. *Phys. Chem. Chem. Phys.* **2011**, *13* (7), 2517–2527.

(12) Carrettin, S.; Concepción, P.; Corma, A.; López Nieto, J. M.; Puntes, V. F. *Angew. Chemie - Int. Ed.* **2004**, *43* (19), 2538–2540.

(13) Yu, H.; Chen, M.; Rice, P. M.; Wang, S. X.; White, R. L. *Nano Lett.* **2005**, *5* (2), 379–382.

(14) Yin, H.; Wang, C.; Zhu, H.; Overbury, S. H.; Sun, S.; Dai, S. *Chem. Commun.* **2008**, No. 36, 4357–4359.

(15) Lee, Y.; Garcia, M. A.; Frey Huls, N. A.; Sun, S. *Angew. Chemie - Int. Ed.* **2010**, *49* (7), 1271–1274.

(16) Kresse, G.; Hafner, J. *Phys. Rev. B* **1993**, *48*, 13115–13118.

(17) Kresse, G.; Hafner, J. *Phys. Rev. B* **1994**, *49*, 14251–14269.

(18) Kresse, G.; Furthmüller, J. *Comput. Mater. Sci.* **1996**, *6*, 15–50.

(19) Blöchl, P. E. *Phys. Rev. B* **1994**, *50*, 17953–17979.

(20) Kresse, G.; Joubert, D. *Phys. Rev. B* **1999**, *59*, 1758–1775.

(21) Marsman, M.; Kresse, G. *J. Chem. Phys.* **2006**, *125*, 104101.

(22) Perdew, J. P.; Burke, K.; Ernzerhof, M. *Phys. Rev. Lett.* **1997**, *78* (7), 1396.

(23) Perdew, J.; Burke, K.; Ernzerhof, M. *Phys. Rev. Lett.* **1996**, *77* (18), 3865–3868.

(24) Anisimov, V. I.; Zaanen, J.; Andersen, O. K. *Phys. Rev. B* **1991**, *44* (3), 943–954.

(25) Liechtenstein, A. I.; Anisimov, V. I.; Zaanen, J. *Phys. Rev. B* **1995**, *52* (8), R5467--R5470.

(26) Dudarev, S. L.; Botton, G. A.; Savrasov, S. Y.; Humphreys, C. J.; Sutton, A. P. *Phys. Rev. B* **1998**, *57* (3), 1505–1509.

(27) Bengone, O.; Alouani, M.; Blöchl, P.; Hugel, J. *Phys. Rev. B* **2000**, *62* (24), 16392–16401.

(28) Monkhorst, H. J.; Pack, J. D. *Phys. Rev. B* **1976**, *13*, 5188–5192.

(29) Reuter, K.; Scheffler, M. *Phys. Rev. B* **2001**, *65* (3), 35406.

(30) Gatel, C.; Snoeck, E. *Surf. Sci.* **2006**, *600* (13), 2650–2662.

(31) Gatel, C.; Snoeck, E. *Surf. Sci.* **2007**, *601*, 1031–1039.

(32) Shaikhutdinov, S. K.; Meyer, R.; Naschitzki, M.; Bäumer, M.; Freund, H. J. *Catal. Letters* **2003**, *86* (4), 211–219.

(33) Santos-Carballal, D.; Roldan, A.; Grau-Crespo, R.; de Leeuw, N. H. *Phys. Chem. Chem. Phys.* **2014**, *16* (39), 21082–21097.

(34) Zhao, L.; Zhang, H.; Xing, Y.; Song, S.; Yu, S.; Shi, W.; Guo, X.; Yang, J.; Lei, Y.; Cao, F. *Chem. Mater.* **2008**, *20* (1), 198–204.

(35) Wahlström, E.; Lopez, N.; Schaub, R.; Thostrup, P.; Rønnau, a; Africh, C.; Laegsgaard, E.; Nørskov, J. K.; Besenbacher, F. *Phys. Rev. Lett.* **2003**, *90* (2), 26101.

(36) Chen, M. S.; Goodman, D. W. *Top. Catal.* **2007**, *44* (1–2), 41–47.

(37) Lee, Y.; He, G.; Akey, A. J.; Si, R.; Flytzani-Stephanopoulos, M.; Herman, I. P. *J. Am. Chem. Soc.* **2011**, *133*, 12952–12955.

(38) McIntyre, N. S.; Zetaruk, D. G. *Anal. Chem.* **1977**, *49* (11), 1521–1529.

(39) Grosvenor, A. P.; Kobe, B. A.; Biesinger, M. C.; McIntyre, N. S. *Surf. Interface Anal.* **2004**, *36* (12), 1564–1574.

(40) Syed, S.; Endo, Y.; Sato, T.; Kawamura, Y.; Nakatani, R. *Mater. Trans.* **2008**, *49* (1), 175–178.

(41) Jayne, D. T.; Fatemi, N. S.; Weizer, V. G. *J. Vac. Sci. Technol. A Vacuum, Surfaces, Film.* **1991**, *9* (3), 1410–1415.